Mirau-based line-field confocal optical coherence tomography

Arnaud Dubois, Weikai Xue, O Levecq, P Bulkin, Anne-Lise Coutrot, Jonas Ogien

Research Article | Vol. 28, No. 6 / 16 March 2020 / Optics Express 7918
Optics EXPRESS

Mirau-based line-field confocal optical coherence tomography

ARNAUD DUBOIS,[1,2,*] WEIKAI XUE,[1] O. LEVECQ,[2] P. BULKIN,[3] ANNE-LISE COUTROT,[1] AND JONAS OGIEN[2]

[1] *Université Paris-Saclay, Institut d'Optique Graduate School, CNRS, Laboratoire Charles Fabry, 91127 Palaiseau, France*
[2] *DAMAE Medical, 28 rue de Turbigo, 75003 Paris, France*
[3] *LPICM, CNRS, Ecole polytechnique, Institut Polytechnique de Paris, 91128 Palaiseau, France*
[*] *arnaud.dubois@institutoptique.fr*

Abstract: Line-field confocal optical coherence tomography (LC-OCT) is an imaging technique in which A-scans are acquired in parallel through line illumination with a broadband laser and line detection with a line-scan camera. B-scan imaging at high spatial resolution is achieved by dynamic focusing in a Linnik interferometer. This paper presents an LC-OCT device based on a custom-designed Mirau interferometer that offers similar spatial resolution and detection sensitivity. The device has the advantage of being more compact and lighter. *In vivo* imaging of human skin with a resolution of 1.3 µm × 1.1 µm (lateral × axial) is demonstrated over a field of 0.9 mm × 0.4 mm (lateral × axial) at 12 frames per second.

1. Introduction

Line-field confocal optical coherence tomography (LC-OCT) is a recently introduced interferometric imaging technique, based on the time-domain version of optical coherence tomography (OCT) [1], with line illumination of the sample and line detection of the signal instead of point scanning and point detection as in conventional OCT [2]. LC-OCT produces B-scans from multiple A-scans acquired in parallel using a line camera. The focus is continuously adjusted during the scan of the sample depth, allowing the use of a high numerical aperture (NA) microscope objective to image with high lateral resolution. By using a supercontinuum laser as a broadband light source and balancing the chromatic dispersion in the interferometer arms, the axial resolution is similar to the lateral resolution, i.e. ~ 1 µm at a central wavelength of ~ 800 nm [2]. This is comparable to the best resolution reported so far in OCT at the same central wavelength [3].

The concept of line illumination of the sample in OCT to avoid lateral scanning of a light beam has also been implemented in frequency-domain OCT (FD-OCT). Several spectrometer-based line-field FD-OCT systems have been reported, allowing the acquisition of a B-scan in a single shot [4–7]. Line-field FD-OCT systems using a swept-laser source have also been developed, with advantages compared to spectrometer-based line-field FD-OCT, including reduced sensitivity roll-off and less influence of scattering crosstalk [8]. Three-dimensional imaging was achieved with swept-source line-field FD-OCT using commercially available components, with competitive sensitivity, speed, image contrast and penetration depth compared to conventional point-scanning FD-OCT [9].

Line-field FD-OCT has a significant advantage over LC-OCT in image acquisition speed. LC-OCT acquires B-scans at a rate of ~ 10 Hz, which about 100 times slower than high-speed line-field FD-OCT (considering the same number of pixels per B-scan) [9]. However, FD-OCT suffers an inherent limitation in lateral resolution since the focus cannot be adjusted during the parallel acquisition of the information in depth. Despite efforts to minimize this limitation, the lateral resolution in FD-OCT is limited to a few micrometers [10–12].

#389637 https://doi.org/10.1364/OE.389637
Journal © 2020 Received 4 Feb 2020; accepted 6 Feb 2020; published 2 Mar 2020

Optics EXPRESS

A major interest of LC-OCT, as a time-domain OCT (TD-OCT) technique, is the possibility to continuously adjust the focus as a function of depth, since the depth information is acquired sequentially. Although it is one of the most efficient method to optimize the lateral resolution, dynamic focusing in conventional point-scanning TD-OCT is challenging for real-time imaging since both a tracking speed on the order of a few m/s and a repetition rate in the kilohertz range are needed [13–16]. In LC-OCT, the parallel acquisition of the A-scans allows a reduction in depth scanning speed without increasing the image acquisition time. Dynamic focusing is therefore highly facilitated in LC-OCT compared to point-scanning TD-OCT.

On the other hand, LC-OCT benefits from a confocal gate obtained with the line-scan camera that is optically conjugated with the illumination line to act as a confocal slit, along with the use of a relatively high NA microscope objective [2,17,18]. The confocal gate in LC-OCT, although less efficient than with point scanning and point detection, is beneficial for the imaging penetration depth in scattering samples [2,19]. Despite the lower detection sensitivity of TD-OCT over FD-OCT [20], the more efficient confocal spatial filtering enables LC-OCT to image in highly scattering tissues such as skin to a depth approaching that reached by FD-OCT [21]. In skin tissues, for example, the effective imaging penetration depth of LC-OCT is ~ 400 µm, which allows to image with a cellular-level spatial resolution down to a depth beyond the dermal-epidermal junction [22,23].

The LC-OCT prototypes reported so far were all based on a Linnik-type interferometer using two identical immersion microscope objectives, one placed in the reference arm of the interferometer and the other one in the sample arm [2,22–25]. In order to produce a B-scan in LC-OCT, the coherence plane (plane orthogonal to the optical axis of the objective that corresponds to a zero optical path difference) is scanned in depth while adjusting the focus. This means that the focal plane of the microscope objective in the sample arm must be superimposed with the coherence plane while the sample depth is scanned. Two scanning methods have been reported so far (see Fig. 1). In the method shown in Fig. 1(a), two independent motorized displacements are used, one to vary the length of the reference arm (displacement of the reference objective (MO2) and reference mirror (RM) together) to control the position of the coherence plane and the other one to move the microscope objective in the sample arm (MO1) so as to maintain the focus in the coherence plane [2,24]. In the method shown in Fig. 1(b), (a) single motorized displacement is used. The whole interferometer is moved, the length of the reference

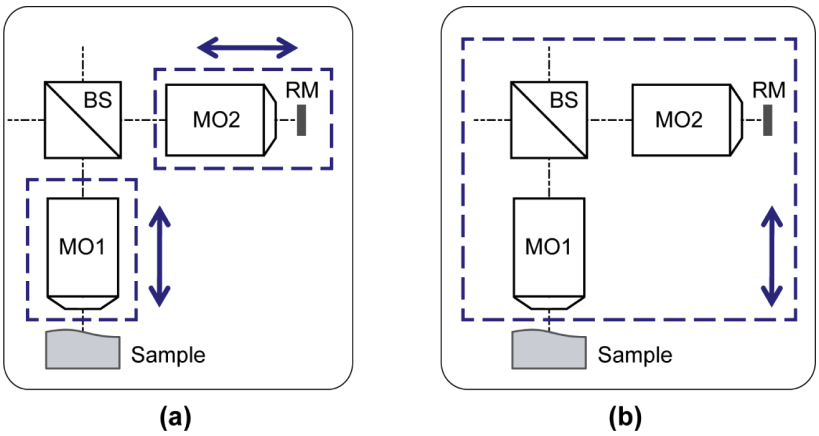

Fig. 1. Schematic representation of elements to move in LC-OCT devices based on the Linnik interferometer for B-scan imaging. MO1, MO2: microscope objectives; BS: beam splitter; RM: reference mirror.

Optics EXPRESS

arm being constant [22]. In both methods, immersion microscope objectives are employed with an immersion liquid of refractive index similar to the one of the sample. This keeps the chromatic dispersion identical in both arms of the interferometer during the scan of the sample depth [26]. This also allows keeping the superimposition of the coherence and focus planes when only one displacement is used [Fig. 1(b)] [26–28]. However, the experimental configurations of the LC-OCT devices reported so far have several drawbacks, including size and weight. Based on a Linnik interferometer, an LC-OCT device cannot be designed very compact and light, especially when two motorized displacements are used [Fig. 1(a)]. In the most compact configuration using a single displacement [Fig. 1(b)], the entire Linnik interferometer is moved [22]. Due to inertia, the acceleration of the motorized translations is limited. B-scans over a depth range of 500 µm were then acquired at a maximal rate of ~ 10 Hz [22].

Using a single microscope objective rather than two would reduce the drawbacks of Linnik-based LC-OCT devices in terms of size, weight and limitation in image acquisition speed. Two-waves interference microscopes using a single objective could be used such as the Michelson interference microscope and the Mirau interference microscope (see Fig. 2). These interference microscopes are commercially available for use in air with dry objectives. Custom-designed Mirau and Michelson interference objectives for use with an immersion liquid have been reported [29–32].

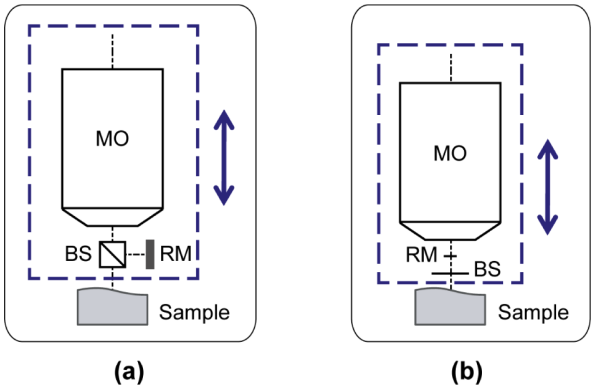

Fig. 2. Michelson (a) and Mirau (b) interference objectives incorporating a microscope objective (MO), a beam-splitter (BS) and a reference mirror (RM). The interference objectives are displaced axially to scan the sample depth.

We present in this paper a LC-OCT device based on a custom-designed immersion interference objective. The Mirau configuration rather than the Michelson configuration was chosen since it is more compact and permits the use of a microscope objective with a higher numerical aperture. The design of the Mirau interferometer and of the whole LC-OCT setup is described. The performance of the device is characterized in terms of detection sensitivity and spatial resolution. An image of human skin is shown as an illustration of the performance of the device for biological tissue imaging *in vivo*.

2. Mirau-based LC-OCT setup

A schematic of our Mirau interferometer is shown in Fig. 3(a). It consists of a custom-designed interferometric attachment mounted to a threaded water immersion microscope objective. The attachment contains a beam-splitter and a reference mirror (RM). The reference mirror is made of gold deposited in the center of the lower surface of a 200 µm-thick fused silica plate. The gold deposit has a rectangular shape (100 µm × 2 mm) and a thickness of about 200 nm. The

Optics EXPRESS

beam-splitter is fabricated from a 500 μm-thick fused silica plate with a dielectric coating deposited on the lower surface. The coating is a ~ 10 nm-thick layer of hydrogenated amorphous silicon (a-SiH). The distance between the two plates is 1 mm. The position of the interferometric attachment is adjusted so that the reference mirror is located in the focal plane of the objective after reflection on the coated surface of the beam-splitter. The reference mirror and the sample are both illuminated by a line of light focused by the microscope objective. Immersion liquid is introduced between the two glass plates and between the objective and the upper plate. A water-immersion microscope objective with a working distance of 3.5 mm was selected to accommodate the beam-splitter and the reference mirror (Olympus UMPLFLN 20xW, NA = 0.5).

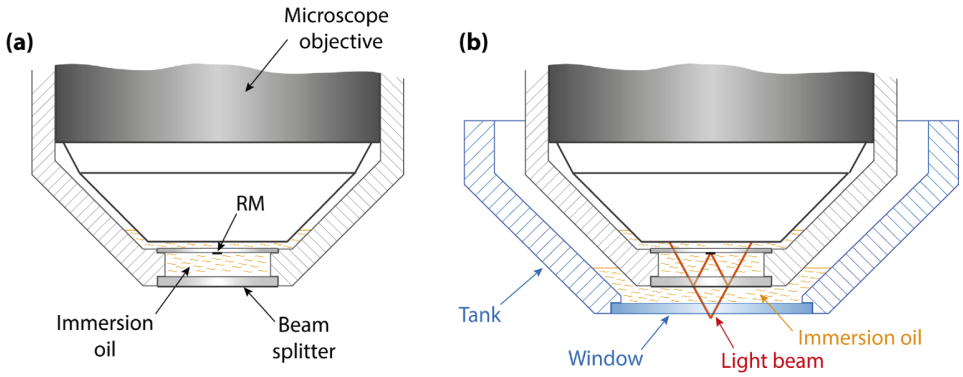

Fig. 3. (a) Schematic of the custom-designed immersion Mirau interferometer. The interferometric attachment, mounted to a threaded water immersion microscope objective, contains a beam splitter and a reference mirror (RM). It is filled with immersion oil. (b) Schematic of the Mirau interferometer immersed in a tank filled with immersion oil. The bottom of the tank has a glass window. The Mirau interferometer is displaced axially to image inside the sample placed against the window.

The Mirau interferometer is partially immersed in a tank filled with immersion liquid [see Fig. 3(b)]. The bottom of the tank has a 500 μm-thick fused silica window. The Mirau interferometer is axially displaced to vary the depth at which the illumination line is focused in the sample placed against the window. This configuration is analog to that with displacement of the whole Linnik interferometer [Fig. 1(b)]. An immersion medium with a refractive index similar to that of the sample is used to minimize the chromatic dispersion mismatch in the interferometer and maintain the superposition of the coherence and focus planes as the imaging depth in the sample is increased [26]. Silicone oil (refractive index of $n \sim 1.4$) is used as immersion medium for skin tissue imaging.

The layout of the Mirau-based LC-OCT device is shown in Fig. 4. A supercontinuum laser source (Leukos, SMHP-80.2) is used to generate spatially coherent ultra-broadband light. The TEM00 laser beam at the output of the nonlinear fiber (NLF) is collimated using an achromatic collimator. After being partially reflected by a broadband polarizing beam-splitter cube (PBS), the beam is linearly polarized. Before entering the Mirau interferometer, the beam is circularly polarized using an achromatic quarter-wave plate (QWP) (Thorlabs AQWP10M-980). Line illumination of the sample is achieved using a plano-convex cylindrical lens (CL) of 50 mm focal length placed before the cube beam-splitter. Light returning from the Mirau interference objective, totally transmitted by the quarter wave plate (QWP) and the polarizing beam-splitter (PBS), is projected using a 200 mm-focal length tube lens (TL), onto a 2048 pixel, 12 bit, line-scan CMOS camera (e2v, Octoplus). The Mirau interference objective is mounted on a piezoelectric-driven linear stage (PZT) (Physik Instrument, P625.1CD) to scan the sample depth.

Optics EXPRESS

Since the objective is infinite conjugate, the image is always focused on the camera sensor during the axial scan of the Mirau objective.

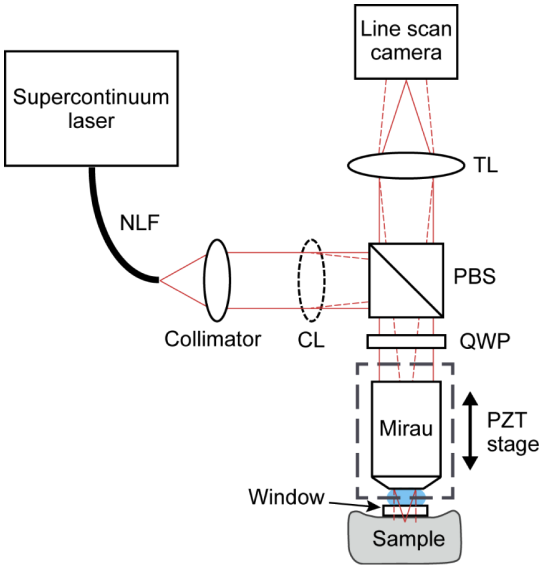

Fig. 4. Layout of the Mirau-based LC-OCT device. The Mirau interferometer is mounted on a piezoelectric (PZT) translation stage (gray dashed frame) for scanning the sample depth. NLF: nonlinear fiber; CL: cylindrical lens; PBS: polarization beam-splitter; QWP: quarter-wave plate; TL: tube lens. The solid red lines represent the beam in the plane of the figure (the cylindrical lens has no effect in this plane). The dotted red lines represent the beam in the direction orthogonal to the plane of the figure.

The PZT stage oscillates in an asymmetric triangular manner with an amplitude of $Z = 400$ µm at a frequency $f_{PZT} = 1/T = 12$ Hz (see Fig. 5). The frequency f_{cam} of the camera is adjusted so that an optical phase-shift of $\sim \pi/2$ is generated in the interferometer between the acquisitions of two consecutive lines, which corresponds to a displacement of the PZT stage of $\delta = \lambda/8n$. The mean optical wavelength of the detected light being $\lambda = 800$ nm and the refractive index $n \sim 1.4$, the frequency of the camera is set to

$$f_{cam} = \frac{Z}{0.8\ \delta} f_{PZT} = 84\ kHz. \tag{1}$$

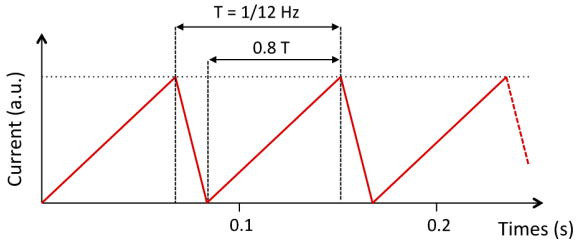

Fig. 5. Periodic current driving the oscillation of the piezoelectric stage. The asymmetric triangle signal has a frequency of $f_{PZT} = 1/T = 12$ Hz and a duty cycle of 80%. Only images acquired during the slow positive ramps are used.

Optics EXPRESS

A stack of $Z/\delta = 5,600$ lines is acquired during each slow depth scan. A B-scan image is obtained by processing the acquired stack using a five-frame fringe envelope detection algorithm [33]. Acquisition and processing of stacks is repeated continuously during the round-trips of the PZT stage. The calculation of the B-scan images is performed with a field-programmable gate array (FPGA). The images are displayed in real-time at ~ 12 frames/s in logarithmic scale with auto-adjusted contrast after being appropriately rescaled. The size of each B-scan is 2048×910 pixels (lateral $\times$ axial), corresponding to a field of view of 0.9 mm $\times$ 0.4 mm (lateral $\times$ axial).

3. Performance

3.1. Detection sensitivity

Neglecting the detection of residual reflections on the antireflection-coated optical surfaces in the device, the intensities of the reference and sample waves on the detector can be written respectively as

$$I_{Ref} = (I_0/2)B_{BS}^2 R_{Ref}, \tag{2.1}$$

and

$$I_S = (I_0/2)(1 - R_{BS})^2 R_S, \tag{2.2}$$

where I_0 is the intensity at the output of the nonlinear fiber (NLF) collected by the collimator. R_{BS} represents the reflectivity of the beam-splitter in the Mirau interferometer and R_{Ref} the reflectivity of the reference mirror. R_S is the global reflectivity of the sample (including both light that is coherent and incoherent with light reflected by the reference mirror). According to the theoretical analysis published in [34–36], the detection sensitivity depends on the ratio of the intensities of the waves returning from each arm of the interferometer. In the Mirau configuration, this ratio is

$$\rho_{Mirau} = \frac{(1 - R_{BS})^2 R_S}{R_{BS}^2 R_{Ref}}. \tag{3}$$

In comparison, the intensities of the reference and sample waves in the Linnik configuration [1,4] are, respectively,

$$I_{Ref,Linnik} = (I_0/4)R_{Ref,Linnik}, \tag{4.1}$$

and

$$I_{S,Linnik} = (I_0/4)R_S, \tag{4.2}$$

where $R_{Ref,Linnik}$ denotes the reflectivity of the reference mirror. The intensity is reduced by a factor of 4 after reflection and transmission by the nonpolarizing beam-splitter of the Linnik interferometer [2]. The ratio of the two waves returning from the Linnik interferometer arms is then

$$\rho_{Linnik} = \frac{R_S}{R_{Ref,Linnik}}. \tag{5}$$

In the Mirau-based device presented here, the reflectivity of the reference mirror is $R_{Ref} = 96\%$ and the reflectivity of the beam-splitter is $R_{BS} = 17\%$. In the Linnik-based LC-OCT devices reported so far, the reflectivity of the reference mirror was $R_{Ref,Linnik} = 4\%$ [2,22]. By substituting these numerical values in Eqs. (3) and (5), it can be seen that $\rho_{\text{Mirau}} \sim \rho_{\text{Linnik}}$. The theoretical detection sensitivity of the Mirau–based LC-OCT device presented in this paper is therefore similar to the one of the previously reported Linnik-based LC-OCT devices assuming a shot-noise limited detection [2].

The experimental detection sensitivity, considered as the inverse of the mean value of the background noise in the images, can be obtained by comparison with the signal measured from an interface with a known reflectivity. Using the plane interface between the glass window of the tank [see Fig. 3(b)] and paraffin oil as a sample with a reflectivity of $\sim 8{\times}10^{-5}$, the detection

Optics EXPRESS

sensitivity was evaluated at 83 dB. This measurement is reported in Fig. 6. The same experiment with a Linnik-based LC-OCT device gave a detection sensitivity value of 86 dB [2]. The slight difference could be explained by the presence of the glass plates and the gold reference mirror in the Mirau interferometer, which generate stronger unwanted reflections.

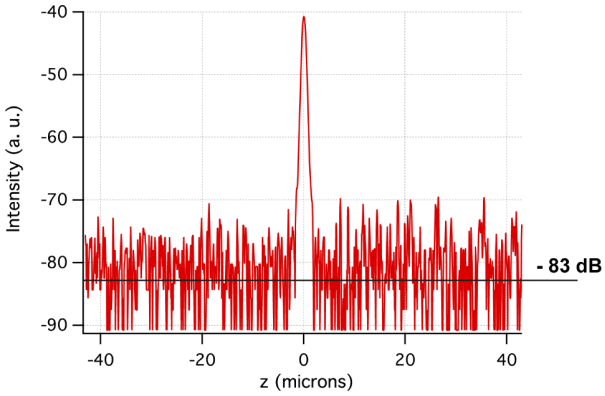

Fig. 6. Axial response to a weak reflectivity (8×10^{-5}) plane interface, calibrated in reflectivity and plotted in decibels (dB). The measured noise-floor (black solid line) corresponds to the opposite of the detection sensitivity.

3.2. *Axial resolution*

The axial response of the Mirau-based LC-OCT device was obtained by imaging the interface between the glass window of the tank [see Fig. 3(b)] and air, without sample. The full-width-at-half-maximum (FWHM) of the imaged interface is 1.10 µm, which is considered to be the axial resolution (see Fig. 7). The theoretical value for the axial resolution, assuming a Gaussian-shaped spectrum centered at 800 nm with a FWHM of 200 nm is 1.00 µm [1]. The difference between theory and experiment is attributed to the influence of the spectral transmittance of the optical components and the non-Gaussian shape of the detected spectrum. The axial resolution is very close to the one measured in the Linnik configuration (1.15 µm) [2].

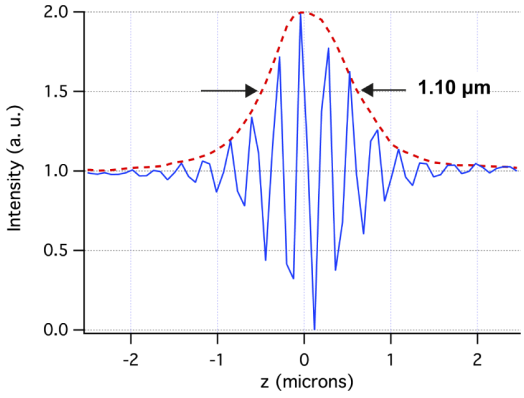

Fig. 7. Measurement of the axial resolution. The red dotted line is the axial response to a plane interface, obtained from digital demodulation of the interference fringes (blue solid line). The axial resolution is defined as the FWHM of the fringe envelope.

Optics EXPRESS

3.3. Lateral resolution

The lateral resolution of the images produced by our Mirau-based LC-OCT device was measured by imaging a high-contrast edge, and recording an intensity profile across it. The 20-80% width of the edge response can be defined as the lateral resolution. It was measured to be 1.3 µm, identical to the one measured with Linnik-based LC-OCT using the same microscope objective [2,22]. Despite central obscuration by the reference mirror of the Mirau interferometer, no significant degradation in lateral resolution was observed. This was to be expected given the geometry and size of the reference mirror (rectangle, 100 µm × 2 mm) compared to the field of view, which produces a slight obscuration (~ 8%). The weak thicknesses of the glass plates placed between the objective and the sample along with the use of oil instead of water as immersion liquid do not seem to generate significant optical aberrations.

It has been shown that the lateral resolution of images acquired in OCT with line-field or full-field illumination of the sample is degraded when spatially-coherent light rather than spatially-incoherent light is used [5,37,38]. This is the result of a phenomenon referred to as optical crosstalk [39]. However, a spatially-coherent light source is required in LC-OCT to efficiently focus the line of light on the sample, with an optical intensity high enough to image at high speed. Besides, the comparison of images acquired in LC-OCT with low spatial coherence illumination or with high spatial coherence illumination shows no obvious difference [2]. This may be due to a less pronounced effect of crosstalk with line-field illumination than with full-field illumination. In addition, movements of the sample may generate random phase variations whose averaging over the interferometric image acquisition time (~ 10 µs) would reduce the effect of crosstalk. This concept has been applied in full-field FD-OCT using a fast deformable membrane that introduces random phase illumination to produce crosstalk free images of human skin [38].

3.4. Imaging

As an illustration of the performance of the device for biological tissue imaging, we considered human skin, *in vivo*. A drop of paraffin oil was added on the skin before it was pressed against the glass window to provide index matching and thus minimize the reflection of light at the interfaces. Figure 8 shows an example image of healthy skin obtained from a 24-year-old man on the back of the hand. The image is the result of an average of 4 B-scans followed by a Gaussian smoothing with a width (standard deviation) of 1 pixel to reduce noise. The image is similar to those obtained with the Linnik-based LC-OCT devices [2,22]. The epidermis and the dermis can be clearly distinguished. They are separated by the dermal-epidermal junction (DEJ). Several layers can be identified in the epidermis: the stratum corneum, the stratum granulosum, the

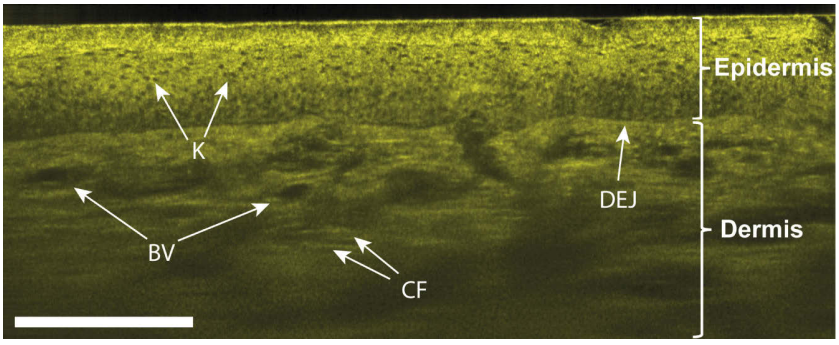

Fig. 8. Image of human skin acquired with Mirau-based LC-OCT. Several skin features are revealed including keratinocytes (K); CF: collagen fibers (CF); blood vessels (BV) and the dermal-epidermal junction (DEJ). Scale bar: 200 µm.

Optics EXPRESS

stratum spinosum, and the stratum basale. The nuclei of keratinocyte cells (K) in the epidermis are resolved and appear as black spots in the image. Collagen fibers (CF) and blood vessels (BV) can be distinguished in the dermis.

4. Conclusion

We have developed an LC-OCT device based on a custom-designed Mirau interferometer that offers similar spatial resolution and detection sensitivity compared to the previously reported LC-OCT devices based on a Linnik interferometer. Mirau-based LC-OCT has the advantage of being more compact and lighter. *In vivo* imaging of human skin with a resolution of 1.3 µm × 1.1 µm (lateral × axial) was demonstrated at 12 frames per second over a field of 0.9 mm × 0.4 mm (lateral × axial).

The frame rate is currently limited at 12 Hz by the mechanical response of the PZT stage to a triangle driving signal and not by camera speed or the power of the light source. We estimate that the frame rate could be increased by a factor of ~ 2 by driving the PZT stage with a sinusoidal signal and operating the camera at a variable frequency in order to maintain a constant phase shift between the acquisition of successive interferometric images.

A compact handheld LC-OCT probe based on the Mirau configuration could be designed for *in vivo* imaging, especially in dermatology. Compared to the LC-OCT devices built so far in the form of an inclinable microscope [22], such a handheld probe would facilitate the use of the LC-OCT technology by dermatologists in daily practice and enable the imaging of difficult-to-access regions of the skin.

Disclosures

The authors declare no conflicts of interest.

References

1. A. Gh. Podoleanu, "Optical coherence tomography," J. Microsc. **247**(3), 209–219 (2012).
2. A. Dubois, O. Levecq, H. Azimani, A. Davis, J. Ogien, D. Siret, and A. Barut, "Line-field confocal time-domain optical coherence tomography with dynamic focusing," Opt. Express **26**(26), 33534–33542 (2018).
3. W. Drexler, U. Morgner, F. Kärtner, C. Pitris, S. Boppart, X. Li, E. Ippen, and J. G. Fujimoto, "*In vivo* ultrahigh-resolution optical coherence tomography," Opt. Lett. **24**(17), 1221–1223 (1999).
4. A. F. Zuluaga and R. Richards-Kortum, "Spatially resolved spectral interferometry for determination of subsurface structure," Opt. Lett. **24**(8), 519–521 (1999).
5. B. Grajciar, M. Pircher, A. Fercher, and R. Leitgeb, "Parallel Fourier domain optical coherence tomography for *in vivo* measurement of the human eye," Opt. Express **13**(4), 1131–1137 (2005).
6. Y. Nakamura, S. Makita, M. Yamanari, M. Itoh, T. Yatagai, and Y. Yasuno, "High-speed three-dimensional human retinal imaging by line-field spectral domain optical coherence tomography," Opt. Express **15**(12), 7103–7116 (2007).
7. S. Lawman, Y. Dong, B. M. Williams, V. Romano, S. Kaye, S. P. Harding, C. Willoughby, Y.-C. Shen, and Y. Zheng, "High resolution corneal and single pulse imaging with line field spectral domain optical coherence tomography," Opt. Express **24**(11), 12395–12405 (2016).
8. M. Mujat, N. V. Iftimia, R. D. Ferguson, and D. X. Hammer, "Swept-source parallel OCT," Proc. SPIE **7168**, 71681E (2009).
9. D. J. Fechtig, B. Grajciar, T. Schmoll, C. Blatter, R. M. Werkmeister, W. Drexler, and R. A. Leitgeb, "Line-field parallel swept source MHz OCT for structural and functional retinal imaging," Biomed. Opt. Express **6**(3), 716–735 (2015).
10. J. P. Rolland, P. Meemon, S. Murali, K. P. Thompson, and K.-S. Lee, "Gabor-based fusion technique for optical coherence microscopy," Opt. Express **18**(4), 3632–3642 (2010).
11. D. J. Fechtig, A. Kumar, W. Drexler, and R. A. Leitgeb, "Full range line-field parallel swept source imaging utilizing digital refocusing," J. Mod. Opt. **62**(21), 1801–1807 (2015).
12. S. Liu, J. A. Mulligan, and S. G. Adie, "Volumetric optical coherence microscopy with a high space-bandwidth-time product enabled by hybrid adaptive optics," Biomed. Opt. Express **9**(7), 3137–3152 (2018).
13. J. M. Schmitt, S. L. Lee, and K. M. Yung, "An optical coherence microscope with enhanced resolving power in thick tissue," Opt. Commun. **142**(4-6), 203–207 (1997).
14. F. Lexer, C. K. Hitzenberger, W. Drexler, S. Molebny, H. Sattmann, M. Sticker, and A. F. Fercher, "Dynamic coherent focus OCT with depth-independent transversal resolution," J. Mod. Opt. **46**(3), 541–553 (1999).

Optics EXPRESS

15. B. Qi, P. A. Himmer, M. L. Gordon, V. X. D. Yang, D. L. Dickensheets, and I. A. Vitkin, "Dynamic focus control in high-speed optical coherence tomography based on a microelectromechanical mirror," Opt. Commun. **232**(1-6), 123–128 (2004).
16. A. Divetia, T.-H. Hsieh, J. Zhang, Z. Chen, M. Bachman, and G.-P. Li, "Dynamically focused optical coherence tomography for endoscopic applications," Appl. Phys. Lett. **86**(10), 103902 (2005).
17. Y. Chen, S.-W. Huang, A. D. Aguirre, and J. G. Fujimoto, "High-resolution line-scanning optical coherence microscopy," Opt. Lett. **32**(14), 1971–1973 (2007).
18. D. S. Gareau, J. G. Krueger, J. E. Hawkes, S. R. Lish, M. P. Dietz, A. G. Mülberger, E. W. Mu, M. L. Stevenson, J. M. Lewin, S. A. Meehan, and J. A. Carucci, "Line scanning, stage scanning confocal microscope (LSSSCM)," Biomed. Opt. Express **8**(8), 3807–3815 (2017).
19. Y. Chen, S.-W. Huang, C. Zhou, B. Potsaid, and J. G. Fujimoto, "Improved detection sensitivity of line-scanning optical coherence microscopy," IEEE J. Sel. Top. Quantum Electron. **18**(3), 1094–1099 (2012).
20. M. A. Choma, M. V. Sarunic, C. Yang, and J. A. Izatt, "Sensitivity advantage of swept source and Fourier domain optical coherence tomography," Opt. Express **11**(18), 2183–2189 (2003).
21. A. Levine, K. Wang, and O. Markowitz, "Optical Coherence Tomography in the Diagnosis of Skin Cancer," Dermatol. Clin. **35**(4), 465–488 (2017).
22. A. Dubois, O. Levecq, H. Azimani, D. Siret, A. Barut, M. Suppa, V. Del Marmol, J. Malvehy, E. Cinotti, and J. L. Perrot, "Line-field confocal optical coherence tomography for high-resolution noninvasive imaging of skin tumors,'," J. Biomed. Opt. **23**(10), 1 (2018).
23. M. Cazalas, O. Levecq, H. Azimani, D. Siret, A. Barut, M. Suppa, V. del Marmol, J. Malvehy, E. Cinotti, P. Rubegni, J. L. Perrot, and A. Dubois, "Skin lesion imaging with line-field confocal optical coherence tomography," in *Photonics in Dermatology and Plastic Surgery 2019*, vol. 10851 B. Choi and H. Zeng, eds., International Society for Optics and Photonics (SPIE, 2019), pp. 61–68.
24. A. Davis, O. Levecq, H. Azimani, D. Siret, and A. Dubois, "Simultaneous dual-band line-field confocal optical coherence tomography. Application to skin imaging," Biomed. Opt. Express **10**(2), 694–706 (2019).
25. J. Ogien, D. Siret, O. Levecq, H. Azimani, A. David, W. Xue, J. L. Perrot, and A. Dubois, "Line-field confocal optical coherence tomography," in *Optical Coherence Tomography and Coherence Domain Optical Methods in Biomedicine XXIII*, J. A. Izatt and J. G. Fujimoto, eds. (SPIE, 2019).
26. A. Dubois, "Focus defect and dispersion mismatch in full-field optical coherence microscopy," Appl. Opt. **56**(9), D142–D150 (2017).
27. A. Dubois, G. Moneron, and A. C. Boccara, "Thermal-light full-field optical coherence tomography in the 1.2 micron wavelength region," Opt. Commun. **266**(2), 738–743 (2006).
28. S. Labiau, G. David, S. Gigan, and A. C. Boccara, "Defocus test and defocus correction in full-field optical coherence tomography," Opt. Lett. **34**(10), 1576–1578 (2009).
29. E. Beaurepaire, A. C. Boccara, M. Lebec, L. Blanchot, and H. Saint-Jalmes, "Full-field optical coherence microscopy," Opt. Lett. **23**(4), 244–246 (1998).
30. O. V. Lyulko, G. Randers-Pehrson, and D. J. Brenner, "Simultaneous immersion Mirau interferometry," Rev. Sci. Instrum. **84**(5), 053701 (2013).
31. S.-H. Lu, C.-J. Chang, and C.-F. Kao, "Full-field optical coherence tomography using immersion Mirau interference microscope," Appl. Opt. **52**(18), 4400–4403 (2013).
32. C.-C. Tsai, C.-K. Chang, K.-Y. Hsu, T.-S. Ho, M.-Y. Lin, J.-W. Tjiu, and S.-L. Huang, "Full-depth epidermis tomography using a Mirau-based full-field optical coherence tomography," Biomed. Opt. Express **5**(9), 3001–3010 (2014).
33. K. G. Larkin, "Efficient nonlinear algorithm for envelope detection in white light interferometry," J. Opt. Soc. Am. A **13**(4), 832–843 (1996).
34. A. Dubois and A. C. Boccara, (2008) "Full-Field Optical Coherence Tomography," In: W. Drexler and J. G Fujimoto, eds. *Optical Coherence Tomography. Biological and Medical Physics, Biomedical Engineering*. Springer, Berlin, Heidelberg.
35. A. Dubois, K. Grieve, G. Moneron, R. Lecaque, L. Vabre, and C. Boccara, "Ultrahigh-resolution full-field optical coherence tomography," Appl. Opt. **43**(14), 2874–2883 (2004).
36. A. Dubois, L. Vabre, A. C. Boccara, and E. Beaurepaire, "High-resolution full-field optical coherence tomography with a Linnik microscope,'," Appl. Opt. **41**(4), 805–812 (2002).
37. D. Borycki, M. Hamkało, M. Nowakowski, M. Szkulmowski, and M. Wojtkowski, "Spatiotemporal optical coherence (STOC) manipulation suppresses coherent crosstalk in full-field swept-source optical coherence tomography," Biomed. Opt. Express **10**(4), 2032–2054 (2019).
38. P. Stremplewski, E. Auksorius, P. Wnuk, Ł. Kozoń, P. Garstecki, and M. Wojtkowski, "*In vivo* volumetric imaging by crosstalk-free full-field OCT," Optica **6**(5), 608–617 (2019).
39. B. Karamata, M. Laubscher, P. Lambelet, R. P. Salathé, and T. Lasser, "Spatially incoherent illumination as a mechanism for crosstalk suppression in wide-field optical coherence tomography," Opt. Lett. **29**(7), 736–738 (2004).